

# Homojunction internal photoemission far-infrared detectors: Photoresponse performance analysis

A. G. U. Perera, H. X. Yuan, and M. H. Francombe

*Department of Physics and Astronomy, Georgia State University, Atlanta, Georgia 30303*

(Received 16 May 1994; accepted for publication 5 October 1994)

The concept of homojunction internal photoemission far-infrared (FIR) detectors has been successfully demonstrated using forward biased Si *p-i-n* diodes at 4.2 K. The basic structure consists of a heavily doped IR absorber layer and an intrinsic (or lightly doped) layer. An interfacial workfunction between these regions defines the long-wavelength cutoff ( $\lambda_c$ ) of the detector. Three types of detectors are distinguished according to the emitter layer doping concentration level. Our model shows that high performance Si FIR detectors ( $>40 \mu\text{m}$ ) can be realized using the type-II structures with a tailorable  $\lambda_c$ , in which the absorber/emitter layer is doped to a level somewhat above the metal-insulator transition value. Analytic expressions are used to obtain the workfunction versus doping concentration, and to describe the carrier photoemission processes. The photoexcitation due to free-carrier absorption, emission to the interfacial barrier, hot-carrier transport, and barrier collection due to the image force effect, are considered in calculating the spectral response and quantum efficiency as functions of device parameters for Si  $n^+-i$  structures, leading to a detailed photoresponse analysis of type-II detectors. These results are useful for the design and optimization of type-II detectors. © 1995 American Institute of Physics.

## I. INTRODUCTION

In recent years, there has been a great need to develop far-infrared (FIR) detectors for space astronomy applications, such as the Space Infrared Telescope Facility (SIRTF).<sup>1</sup> The conventional detectors used for the 40–200  $\mu\text{m}$  wavelength range are extrinsic Ge photoconductors, such as unstressed Ge:Ga devices for the 40–120  $\mu\text{m}$  and stressed Ge:Ga for the 120–200  $\mu\text{m}$ .<sup>2</sup> Ge blocked-impurity-band (BIB) detectors<sup>3,4</sup> are also under development in order to overcome the limitations inherent in conventional extrinsic photoconductors and extend the cutoff wavelength ( $\lambda_c$ ). However, at present, no Si FIR detectors exist that can operate effectively beyond 40  $\mu\text{m}$  at low backgrounds.<sup>5</sup> In this paper, we present an analytic model for a novel Si homojunction internal photoemission FIR detector, with high performance and a tailorable  $\lambda_c$ .

The concept of homojunction internal photoemission for FIR detection was first proposed and demonstrated on forward biased commercial Si *p-i-n* diodes at 4.2 K.<sup>6</sup> The detector  $\lambda_c$  was extended to very long wavelength range ( $>200 \mu\text{m}$ ), and similar results were also obtained for Ge and InGaAs *p-i-n* diodes.<sup>7</sup> In addition, experimental results obtained with a single  $p^+-i$  interface structure were reported, and the concept of multilayer structures was proposed.<sup>8</sup> Also, similar detector concept was proposed and demonstrated for a Si molecular beam epitaxy (MBE) multilayer structure in the LWIR range.<sup>9</sup> The detection mechanism<sup>6</sup> assumes that the biased interface structure, consisting of a heavily doped IR absorber layer and an intrinsic (or lightly doped) layer ( $n^+-i$  or  $p^+-i$ ), can be depicted as an internal photoemitter at low temperatures ( $\leq 20$  K). For an  $n^+-i$  ( $p^+-i$ ) structure, the Fermi level in the heavily doped layer can lie below (above) the conduction (valence) band edge of the *i* layer, giving rise to an interfacial workfunction, which defines the long-wavelength IR cutoff for the detector. When the doping con-

centration is above the metal-insulator transition (Mott transition) value, the detector can be regarded as a metal photoemitter, which will be called type-II detector in this paper, otherwise it can be regarded as a semiconductor photoemitter (type-I detector). Following a linearly distributed space-charge model,<sup>10</sup> we can show that the space-charge effect at the interface is negligible at low temperatures. As all the experimental results, up to now, were obtained on commercial *p-i-n* diodes which were not designed for IR detectors, detector performance was not high. In order to fabricate detectors with high performance, device parameters should be optimized. This in turn requires a better understanding of the detector photoresponse mechanism and detailed modeling work. The photoresponse mechanism of type-I detectors has been analyzed in another paper.<sup>11</sup> In this paper, our focus is mainly on the type-II detector.

Up to now, several types of internal photoemission IR detectors have been proposed and demonstrated.<sup>12</sup> One important type is metal-semiconductor Schottky barrier IR detectors, such as the most highly developed PtSi/Si detector<sup>13</sup> operating in 3–5  $\mu\text{m}$ . Another type is semiconductor heterojunction IR detectors, such as  $\text{Ge}_x\text{Si}_{1-x}/\text{Si}$  detectors<sup>14,15</sup> developed for 8–14  $\mu\text{m}$  or even longer wavelength. There is also a degenerate Si homojunction detector,<sup>16</sup> which has a response in 1–7  $\mu\text{m}$ . Since the structure of the latter detector is very similar to the detectors investigated in this work, here it is categorized as the type-III. In these detectors, the absorber/photoemitter “electrode” may be a metal, a metal silicide or a degenerate semiconductor. Thus, following the terminology of Lin and Maserjian,<sup>14</sup> we may describe all of these detectors as HIP, i.e. hetero- (or homo-) junction internal photoemission detectors. The actual physical processes taking place in the emitting layer are still not well understood, although several theoretical models<sup>17–21</sup> have been developed to describe the hot carrier photoemission. Some of these models will be followed here, to predict the photore-

sponse performance of our type-II HIP FIR detectors.

One of the key factors for the design of type-II HIP detectors is to determine the doping concentration dependence of the interfacial workfunction (hence  $\lambda_c$ ). The heavy doping effects on semiconductor properties, such as the band-gap narrowing, have been extensively studied, from both theoretical and experimental respects.<sup>22</sup> But the physical mechanism is not yet well understood. Also, there is no experimental data available at present time describing the workfunction dependence on doping concentration above the Mott transition. In this paper, we will follow a theoretical model<sup>23</sup> developed recently, which can give simple but accurate closed form equations for band-gap narrowing, to obtain an approximate relationship of  $\lambda_c$  vs doping concentration for the type-II HIP detector.

This paper is arranged in the following way. In Sec. II, three different types of HIP detectors are compared; In Sec. III, an estimate of the workfunction dependence on the doping concentration above the Mott transition is given. In Sec. IV, an analytic model is introduced to describe the carrier photoemission in single layer ( $n^+ - i$  or  $p^+ - i$ ) type-II HIP detectors, which includes photoexcitation, emission to the interfacial barrier, hot electron transport, and barrier collection. In Sec. V, the spectral response and quantum efficiency are calculated for Si  $n^+ - i$  structures, as functions of device parameters. In Sec. VI, the main results are summarized. Although our analysis is mainly for an  $n^+ - i$  interface structure, the method is also valid for a  $p^+ - i$  structure with trivial modifications.

## II. COMPARISON OF THREE DIFFERENT TYPES OF HIP DETECTORS

The basic structure of HIP detectors consists of a heavily doped layer, which acts as the IR absorber region, and an intrinsic (or lightly doped) layer across which most of the external bias is dropped. According to the doping concentration level in the heavily doped layer, the HIP detectors can be divided into three types as shown in Figs. 1(a)–(c), which show different photoresponse mechanisms and response wavelength ranges.

### A. Type-I HIP detectors: $N_d < N_c$ ( $E_F < E_c^{n^+}$ )

When the doping concentration ( $N_d$ ) in the  $n^+$  layer is high but below the Mott critical value ( $N_c$ ), an impurity band is formed. At low temperatures, the Fermi level is located in the impurity band. The incident FIR light is absorbed due to the impurity photoionization, with a workfunction given by  $\Delta = E_c^{n^+} - E_F$ , where  $E_c^{n^+}$  is the conduction band edge in the  $n^+$  layer. An electric field is formed in the  $i$  layer by an external bias to collect photoexcited electrons generated in the  $n^+$  layer. Obviously, type-I HIP detectors are analogous to semiconductor photoemissive detectors<sup>24</sup> in their operation, which can be described by a three-step process [see Fig. 1(a)].

- (1) Electrons are photoexcited from filled impurity band states below Fermi level into empty states above the conduction band edge.

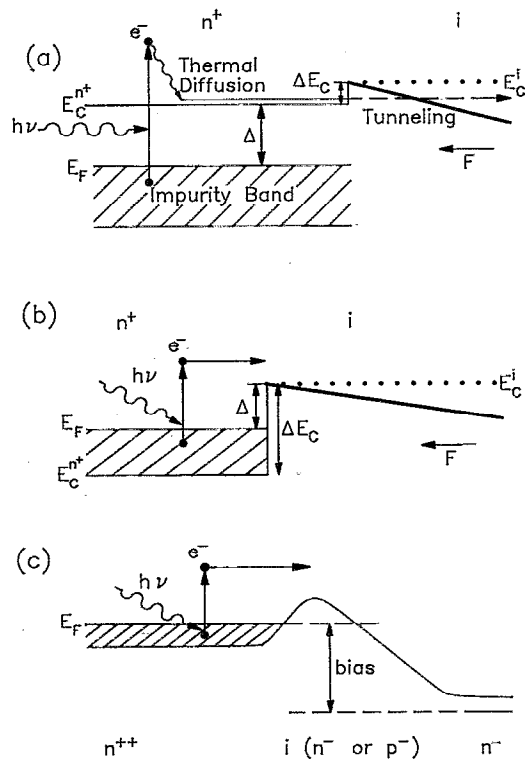


FIG. 1. Energy band diagrams for three different types of HIP detectors. (a) Type I:  $N_d < N_c$  ( $E_F < E_c^{n^+}$ ); (b) Type II:  $N_c < N_d < N_0$  ( $E_c^{n^+} < E_F < E_c^i$ ); (c) Type III:  $N_d > N_0$  ( $E_F > E_c^i$ ). Here,  $N_c$  is the Mott's critical concentration and  $N_0$  is the critical concentration corresponding to  $\Delta = 0$ . In (a) and (b), the conduction band edge of the  $i$  layer is represented by a dotted line for  $V_b = V_0$  (flatband) and by a solid line for  $V_b > V_0$ .

- (2) Photoexcited electrons first rapidly thermalize into the bottom of the conduction band by phonon relaxation and then diffuse to the emitting interface, with the transport probability determined by the electron diffusion length.
- (3) Those electrons reaching the emitting interface tunnel through an interfacial barrier ( $\Delta E_c$ ), which is due to the offset of the conduction band edge caused by the band-gap narrowing effect, and are collected by the electric field in the  $i$  region. The collection efficiency will depend on the tunneling probability which in turn depends on the  $i$  region electric field. The  $\lambda_c$  can be tailorable with the doping concentration to some extent, because with the increase of doping concentration the impurity band broadens and its peak density of state moves towards the conduction band rapidly.<sup>22</sup>

In the above discussion, we have neglected the impurity compensation in the  $n^+$  layer, which is unavoidable for the actual heavily doped semiconductors. Due to the compensation effect, electric field can be induced in the  $n^+$  layer by the external bias. If the compensated acceptor concentration is very small, the electric field region may extend over a large part of the  $n^+$  layer. This is just the case of blocked-impurity-band (BIB) detectors,<sup>25,26</sup> for which the photoexcited electron collection mechanism is different from the pro-

cesses (2) and (3) described in the above paragraph. In contrast to the type-I HIP detector, the BIB detector resembles a reverse-biased photovoltaic detector in its operation, with the collection efficiency in the electric field region approaching 100%. However, if the compensated acceptor concentration is high, in the most part of the  $n^+$  layer there is no electric field induced when an external voltage is applied, except for a very small depletion region near the  $n^+ - i$  interface. In this case, the photoresponse mechanism still can be described by the processes developed above for type-I HIP detectors. Usually, the quantum efficiency of a type-I HIP detector is less than that of a BIB detector due to the nature of internal photoemission. However, when the doping concentration is so high that it is near the Mott transition, technologically it is less likely to get a very low compensated acceptor concentration. So, it is expected that the type-I HIP detector still may have an advantage in a wavelength range longer than that of the BIB detector.

### B. Type-II HIP detector: $N_c < N_d < N_0$ ( $E_c^{n^+} < E_F < E_c^i$ )

When the doping concentration is above the Mott transition, the impurity band is linked with the conduction band edge, and the  $n^+$  layer becomes metallic. Even in this case, the Fermi level can still be below the conduction band edge of the  $i$  layer ( $E_F < E_c^i$ ) due to the band-gap narrowing effect, giving rise to a workfunction  $\Delta = E_c^i - E_F$  as shown in Fig. 1(b), unless  $N_d$  exceeds a critical concentration  $N_0$  at which  $\Delta = 0$ . The workfunction dependence on doping concentration for this case will be discussed in Sec. III. Type-II HIP detectors are analogous to Schottky barrier IR detectors in their operation. One of their unique features is that in principle, there is no restriction on  $\lambda_c$ , which is tailorable in FIR range, because the workfunction can become arbitrary small with increasing doping concentration. This means that we can make Si FIR detectors with any  $\lambda_c$  needed. Unlike type-I HIP detectors, the photon absorption in type-II HIP detectors is due to free-carrier absorption. In spite of the fact of the free carrier absorption coefficient in the metallic  $n^+$  layer is lower than in a metal due to the lower electron concentration, the type-II HIP detector has a higher internal quantum efficiency than the Schottky barrier detector due to the reduction of the Fermi energy. In addition, the hot-electron scattering length in our detectors could be larger than in metals due to the lower electron energy. The photoemission of photoexcited electrons from the  $n^+$  layer into the  $i$  layer is determined by the emission to the interfacial barrier, hot-electron electron transport, and barrier collection process. The emission probability depends on the photon energy and the Fermi energy. The transport probability is governed by various elastic and inelastic hot electron scattering mechanisms occurring in the  $n^+$  layer. The collection efficiency is due to the image force effect at the  $n^+ - i$  interface, which gives rise to a voltage dependence of quantum efficiency. In Sec. IV, an analytic model will be presented to give the related formula for quantum efficiency calculation.

### C. Type-III HIP detector: $N_d > N_0$ ( $E_F > E_c^i$ )

When the doping concentration is so high that the Fermi level is above the conduction band edge of the  $i$  layer, the  $n^+$  layer becomes degenerate, and a barrier associated with a space-charge region is formed at the  $n^+ - i$  interface due to the electron diffusion, as shown in Fig. 1(c). The barrier height depends on the doping concentration and the applied voltage, giving rise to an electrically tunable  $\lambda_c$ . This type of device was first demonstrated by Tohyama *et al.*<sup>16</sup> using a structure composed of a degenerate  $n^{++}$  hot-carrier emitter, a depleted barrier layer (lightly doped  $p$ ,  $n$ , or  $i$ ), and a lightly doped  $n$ -type hot-carrier collector. As the bias voltage is increased, the barrier height is reduced, the spectral response shifts toward longer wavelength, and the signal increases at a given wavelength. The photoemission mechanism of type-III HIP detectors is similar to that of type-II HIP detectors, with the major difference in that they have different response wavelength ranges and different operating temperature ranges. The type-II HIP detector is a FIR detector, and usually operates at temperatures much lower than 77 K. In contrast, the type-III HIP detectors are expected to operate near 77 K and have responses in the MWIR and LWIR ranges.<sup>12</sup>

## III. WORKFUNCTION DEPENDENCE ON DOPING CONCENTRATION ABOVE MOTT TRANSITION

As the doping concentration increases, the impurity band broadens and becomes increasingly asymmetrical, and its peak moves towards the conduction band edge rapidly. At the same time, the conduction band edge also starts moving downwards in the band gap. At the Mott transition concentration, the impurity band and the conduction band merge with each other, and the semiconductor changes from a non-metal to a metal (Mott transition). Above the Mott transition, with further increasing the doping concentration, the impurity band starts to shrink and finally becomes absorbed into the conduction band.<sup>22</sup>

The lowering of the conduction band edge,  $\Delta E_c$ , can be described using the high-density theory. It has been shown<sup>22</sup> that this theory does describe the behavior of heavily doped Si and Ge to a fair degree of accuracy in the high-density regimes, i.e., above the Mott critical concentration, and gives reasonable results even at doping concentrations as low as  $10^{18} \text{ cm}^{-3}$ . The main result of this theory is that the electron-electron interaction (many-body effect) causes a rigid downward shift of the conduction band,  $\Delta E_c^{ex}$ , which is also known as exchange energy. The electron-impurity interaction causes an additional shift,  $\Delta E_c^i$ , and also distorts the density of states function. In this theory, the semiconductor is assumed to be uncompensated and all impurities ionized so that the free-carrier concentration is equal to the doping concentration  $N_d$ . In principle, this theory is valid close to 0 K.

Recently, Jain and Roulston<sup>23</sup> have derived a simple and accurate expression for the shift of the majority band edge,  $\Delta E_{maj}$ , that can be used for all  $n$ - and  $p$ -type semiconductors and for any doping concentration in the high-density regime. By introducing two correction factors to take deviations from

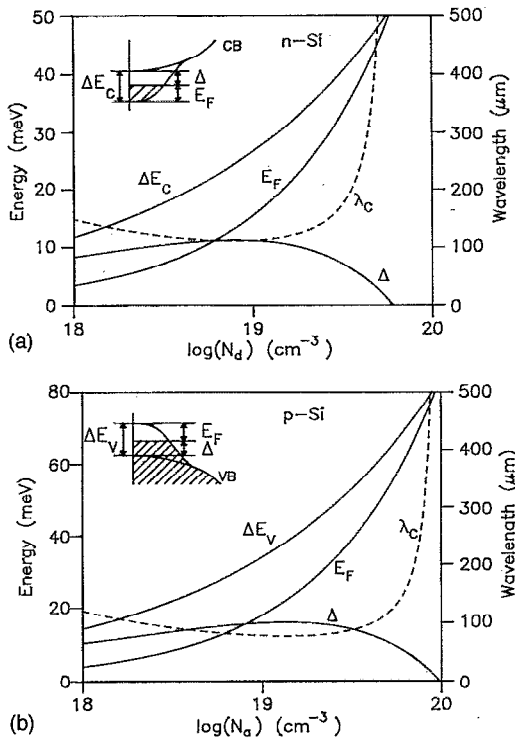


FIG. 2. Doping concentration dependence of  $\Delta E_c$  ( $\Delta E_v$ ),  $E_F$ ,  $\Delta$ , and  $\lambda_c$ , calculated using the high-density theory for (a)  $n$ -type Si and (b)  $p$ -type Si. The insets show the shift of majority band edge and the position of Fermi level, with the shaded areas representing the energy states filled by electrons.

the ideal band structure into account,  $\Delta E_{\text{maj}}$  can be expressed as

$$\Delta E_{\text{maj}} = \Delta E_{\text{maj}}^{\text{ex}} + \Delta E_{\text{maj}}^i, \quad (1)$$

with

$$\Delta E_{\text{maj}}^{\text{ex}} = 1.83\Lambda a \left( \frac{4\pi N}{3N_m} \right)^{1/3} R, \quad (2)$$

$$\Delta E_{\text{maj}}^i = \frac{1.57a}{N_m} \left( \frac{4\pi a N}{3} \right)^{1/2} R,$$

where  $N$  is the doping concentration,  $R = 13.6m_d/\epsilon_s^2$  (eV) is the effective Rydberg energy,  $a = 0.53\epsilon_s/m_d$  (Å) is the effective Bohr radius,  $m_d$  is the effective density-of-state mass, and  $\epsilon_s$  is the relative dielectric constant. The correction fac-

tor  $\Lambda$  takes into account the effect of anisotropy of the bands in  $n$ -type semiconductors and the effect of interactions between the light- and heavy-hole valence bands in  $p$ -type semiconductors.  $N_m$  is the number of conduction band minima in the case of  $n$ -type Si and  $n$ -type Ge, and  $N_m = 2$  for all  $p$ -type semiconductors.

The modified expression for the Fermi energy to take the multiplicity of the majority band into account is given by<sup>27</sup>

$$E_F = \frac{\hbar^2 k_F^2}{2m^*} = \frac{\hbar^2}{2m_d} \left( \frac{3\pi^2 N}{N_m} \right)^{2/3}. \quad (3)$$

So, the workfunction is

$$\Delta = \Delta E_{\text{maj}} - E_F. \quad (4)$$

The cutoff wavelength is given by  $\lambda_c(\mu\text{m}) = 1.24/\Delta(\text{eV})$ .

Using above equations, we have calculated the doping concentration dependence of  $\Delta E_{\text{maj}}$ ,  $E_F$ ,  $\Delta$ , and  $\lambda_c$ . The results for Si (both  $n$  and  $p$  type) are shown in Figs. 2(a) and 2(b). Similar calculations were also performed for Ge and GaAs. The critical concentrations ( $N_0$ ) which correspond to  $\Delta = 0$  can be obtained from the  $\Delta$  vs  $N$  relationships. The Mott critical concentration ( $N_c$ ) can be estimated by using the following approximate expression:<sup>28</sup>

$$N_c^{1/3} a \sim \pi/12 \sim 0.25. \quad (5)$$

Table I shows the values of  $N_0$  and  $N_c$  calculated for both  $n$ - and  $p$ -type Si, Ge, and GaAs, together with the parameters used in the calculation. As discussed in Sec. II B, the type-II HIP detector can operate in the doping concentration range  $N_c < N < N_0$ . Although the actual critical concentrations depend on the impurity selected for doping, above calculations will give an estimate for the workfunction, which is important for the design of type-II HIP detectors.

It is seen from Fig. 2 that as  $N$  approaches  $N_0$ ,  $\lambda_c$  becomes very sensitive to  $N$ , that is, only a small increase in  $N$  can cause a large increase in  $\lambda_c$ . It should be pointed out that although the high-density theory is valid in the high doping range ( $N > N_c$ ), it can not be used for moderately doped semiconductors where  $N$  is in the neighborhood of  $N_c$ .<sup>22</sup> Several properties of moderately doped semiconductors, such as the Fermi level position, the shape of density-of-states which is highly distorted in this case, and the metal-to-nonmetal transition, can not be modeled by this theory. To determine the  $\Delta$  vs  $N$  relationship in the intermediate doping range, other theories, such as Klauder's multiple scattering theory,<sup>29</sup> are needed.

TABLE I. Calculated critical concentrations ( $N_c$  and  $N_0$ ) and parameters used for different semiconductors.

	$n$ -Si	$p$ -Si	$n$ -Ge	$p$ -Ge	$n$ -GaAs	$p$ -GaAs
$\epsilon_s$	11.4	11.4	15.4	15.4	13.0	13.0
$m_d$	0.33	0.59	0.22	0.36	0.0665	0.47
$N_m$	6	2	4	2	1	2
$\Lambda$	1	0.75	0.84	0.75	1	0.75
$R(\text{meV})$	34.5	61.7	12.6	20.6	5.4	38.1
$a(\text{Å})$	18.3	10.2	37.1	22.7	103.6	14.6
$N_c(\text{cm}^{-3})$	$2.55 \times 10^{18}$	$1.47 \times 10^{19}$	$3.06 \times 10^{17}$	$1.34 \times 10^{18}$	$1.41 \times 10^{16}$	$5.02 \times 10^{18}$
$N_0(\text{cm}^{-3})$	$6 \times 10^{19}$	$1 \times 10^{20}$	$3.5 \times 10^{18}$	$8.1 \times 10^{18}$	$1.5 \times 10^{17}$	$3.3 \times 10^{19}$

A. Photoexcitation

A single  $n^+i$  (or  $p^+i$ ) structure consists of three layers (see Fig. 3): the heavily doped emitter layer, the intrinsic (or lightly doped) layer, and the bottom contact layer, with thicknesses  $W_d$ ,  $W_i$ , and  $W_b$ , doping concentrations  $N_d$ ,  $N_i$ , and  $N_b$ , and absorption coefficients  $\alpha_d$ ,  $\alpha_i$ , and  $\alpha_b$ , respectively. The photoexcited electrons generated in the bottom contact layer make no contribution to the photocurrent, hence the light flux  $I_0$  should be incident normally from the top side to reduce the absorption in the bottom contact. The front and back reflectances are  $R_F$  and  $R_B$ , respectively, whose variation with wavelength can be ignored. If the multiple internal reflection effect is considered, the generation rate of photoexcited electrons is given by

$$\eta_a = \int_0^{W_d} G(x) dx / I_0 = \frac{(1 - R_F) \{1 + R_B \exp[-(\alpha_d W_d + 2\alpha_b W_b)]\} [1 - \exp(-\alpha_d W_d)]}{1 - R_F R_B \exp[-2(\alpha_d W_d + \alpha_b W_b)]} \quad (7)$$

One special case is that as  $\alpha_b W_b \rightarrow \infty$ ,  $\eta_a \rightarrow (1 - R_F) [1 - \exp(-\alpha_d W_d)]$ . Another special case is that for  $R_F \rightarrow 0$  and  $R_B \rightarrow 1$  (by using antireflection coating and optical cavity),  $\eta_a \rightarrow \{1 + \exp[-(\alpha_d W_d + 2\alpha_b W_b)]\} [1 - \exp(-\alpha_d W_d)]$ . To reduce the effect of the bottom contact layer, we should, as far as possible, decrease  $\alpha_b$  (by lowering  $N_b$ ) and  $W_b$ .

Infrared absorption experiments done in the range of 2.5–40  $\mu\text{m}$ <sup>30</sup> have shown that for heavily doped Si, the free carrier absorption coefficient is roughly proportional to the free carrier density and the square of the wavelength, and can be described by the following classical expression<sup>31</sup>

$$\alpha = \frac{q^3 \lambda^2 N}{4 \pi^2 \epsilon_0 c^3 n m^{*2} \mu} \quad (8)$$

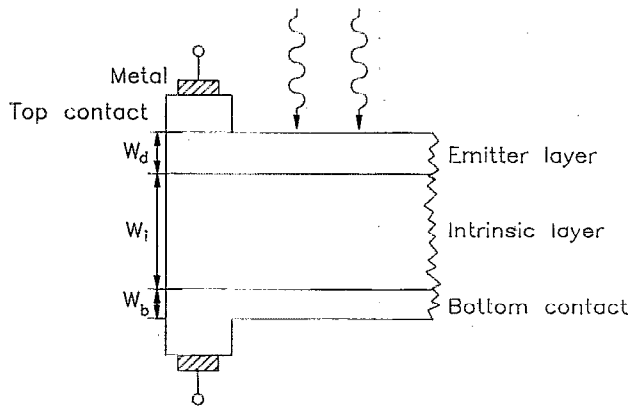


FIG. 3. Basic structure of frontside illuminated type-II HIP detector. In order to reduce the FIR absorption loss in the contact layers, the top (bottom) contact layer under (above) the metal plate can be formed as a ring surrounding the photosensitive area, and the bottom contact layer within the active area should be made as thin as possible. The absorption efficiency in the emitter layer can be increased by the multiple internal reflection.

$$G(x) = G_1 \exp(-\alpha_d x) + G_2 \exp(\alpha_d x), \quad (6)$$

where

$$G_1 = \frac{\alpha_d I_0 (1 - R_F)}{1 - R_F R_B \exp[-2(\alpha_d W_d + \alpha_i W_i + \alpha_b W_b)]}$$

$$G_2 = G_1 R_B \exp[-2(\alpha_d W_d + \alpha_i W_i + \alpha_b W_b)].$$

The FIR absorption in the  $i$  layer can be neglected due to the fact that  $\alpha_i W_i \ll \alpha_d W_d$ ,  $\alpha_b W_b$ . The photon absorption probability, defined as the ratio of the number of photoexcited electrons generated in the emitter layer to the number of incident photons, is

where  $\lambda$  = wavelength,  $N$  = density of free carriers, which is also the doping concentration in our case,  $n$  = refractive index,  $m^*$  = effective mass, and  $\mu$  = mobility. The scattering mechanism involved in the free carrier absorption process can be due to phonon scattering and/or impurity scattering. For  $n$ - and  $p$ -type Si, if we choose the following reasonable values<sup>30</sup> for  $m^*$  and  $\mu$ :  $m_n^*/m_0 = 0.28$  and  $m_p^*/m_0 = 0.37$ ,  $\mu_n \approx 100 \text{ cm}^2/\text{V s}$  and  $\mu_p \approx 50 \text{ cm}^2/\text{V s}$ , then the room temperature absorption coefficients become

$$\begin{aligned} \alpha_n &\approx 2 \times 10^{-18} \lambda^2 N_d, \\ \alpha_p &\approx 1.5 \times 10^{-18} \lambda^2 N_a, \end{aligned} \quad (9)$$

where  $\lambda$  is in  $\mu\text{m}$ . In the heavily doped case, the absorption coefficient varies very little with temperature as demonstrated by experiments,<sup>30</sup> since both carrier concentration and mobility are reasonably invariant with temperature. As no absorption data are available for the wavelength range  $\lambda > 40 \mu\text{m}$ , we will assume that Eq. (9) is still valid for our type-II HIP detectors.

B. Ideal internal photoemission

Now let us consider an ideal case in which there are no collisions of hot electrons or energy losses before they reach the interface, and also no other effects to restrict the emission of electrons over the interfacial barrier. The ideal internal quantum efficiency is defined as the ratio of the number of hot electrons ( $N$ ) emitted over the interfacial barrier to the number of photoexcited electrons ( $N_T$ ), that is,

$$\eta_{id} = N/N_T. \quad (10)$$

The ideal internal photoemission process is usually described by an escape cone model.<sup>32</sup> The main idea is that, due to the fact that the photoexcited electrons have no preferred direction of motion, an electron can escape over the

interfacial barrier only if it has a component of momentum normal to the interface which is greater than  $p_0$ , where  $p_0^2 = 2m^*(E_F + \Delta)$ . This defines an escape cone of velocities or momenta, so any electron moving in a direction lying outside the cone will not be able to escape. The fraction  $f(p)$  of all electrons having momentum  $p$ , which are moving in directions inside the escape cone, is simply the ratio of the surface area of the sphere included within the cone to the total sphere surface area. For an isotropic momentum distribution,

$$f(p) = \frac{1}{2}(1 - p_0/p). \quad (11)$$

If written as a function of energy, this escape probability becomes

$$f(E) = \frac{1}{2} \left( 1 - \sqrt{\frac{E_F + \Delta}{E}} \right). \quad (12)$$

In the zero-temperature approximation,  $N_T$  and  $N$  are given by

$$N_T = \int_{\max(E_F, h\nu)}^{E_F + h\nu} \frac{dN}{dE} dE, \quad (13)$$

$$N = \int_{\max(E_F + \Delta, h\nu)}^{E_F + h\nu} \frac{dN}{dE} f(E) dE, \quad (14)$$

where  $h\nu$  is the photon energy and  $dN/dE$  is the density of states. For our case,  $dN/dE$  can be approximated by  $dN/dE \approx CE^{1/2}$ , where  $E$  is the electron energy relative to the conduction band edge and  $C$  is an energy-independent constant.

If the effects of various scattering processes are considered as discussed in Sec. IV C, even those hot electrons whose momenta are not in the escape cone also have the probability to be redirected into the cone, so that emission is possible. The maximum internal quantum efficiency is given by the ratio of the number of potentially capturable electrons ( $N_M$ ) to the number of photoexcited electrons,

$$\eta_M = N_M/N_T, \quad (15)$$

with

$$N_M = \int_{\max(E_F + \Delta, h\nu)}^{E_F + h\nu} \frac{dN}{dE} dE. \quad (16)$$

By using above equations, analytic expressions of  $\eta_{id}$  and  $\eta_M$  can be easily derived, which are given as follows.

For  $\Delta < h\nu < E_F$  (if  $\Delta < E_F$ ),

$$\eta_{id} = \frac{3}{4} \frac{[(E_F + h\nu)^{3/2} - (E_F + \Delta)^{3/2}] - (h\nu - \Delta)(E_F + \Delta)^{1/2}}{(E_F + h\nu)^{3/2} - E_F^{3/2}}, \quad (17)$$

$$\eta_M = \frac{(E_F + h\nu)^{3/2} - (E_F + \Delta)^{3/2}}{(E_F + h\nu)^{3/2} - E_F^{3/2}}. \quad (18)$$

For  $E_F < h\nu < E_F + \Delta$  (or  $\Delta < h\nu < E_F + \Delta$  if  $E_F < \Delta$ ),

$$\eta_{id} = \frac{3}{4} \frac{[(E_F + h\nu)^{3/2} - (E_F + \Delta)^{3/2}] - (h\nu - \Delta)(E_F + \Delta)^{1/2}}{(E_F + h\nu)^{3/2} - (h\nu)^{3/2}}, \quad (19)$$

$$\eta_M = \frac{(E_F + h\nu)^{3/2} - (E_F + \Delta)^{3/2}}{(E_F + h\nu)^{3/2} - (h\nu)^{3/2}}. \quad (20)$$

For  $h\nu > E_F + \Delta$ ,

$$\eta_{id} = \frac{3}{4} \frac{[(E_F + h\nu)^{3/2} - (E_F + \Delta)^{3/2}] - E_F(E_F + \Delta)^{1/2}}{(E_F + h\nu)^{3/2} - (h\nu)^{3/2}}, \quad (21)$$

$$\eta_M = 1. \quad (22)$$

The internal quantum efficiency expression given above is different from that of Schottky barrier detectors where  $E_F \gg h\nu$  (Ref. 19) or that of  $\text{Ge}_x\text{Si}_{1-x}/\text{Si}$  heterojunction detectors where  $E_F \ll h\nu$ .<sup>15</sup> For the type-II HIP detector, the comparability of  $E_F$  and  $\Delta$  could result in different  $\eta_{M(i)}$  vs  $h\nu$  relationship in different photon energy ranges, which will be seen in Sec. V.

### C. Hot-electron transport

Photoexcited electrons reach the interface for emission either by direct transfer or by scattering towards the interface. Most of hot electrons are lost for emission because they travel in the wrong direction, they lose energy by inelastic scattering, or they are scattered away from the emission barrier. There are also scattering paths that redirect electrons into the escape cone so that emission is possible. Several theoretical models have been developed to describe hot-electron transport in Schottky barrier detectors.<sup>17-19,21</sup> Here, we will basically follow a simplified Vickers-Mooney model<sup>18,19</sup> to get an estimate for the real internal quantum efficiency of our type-II HIP detectors.

We consider three major scattering processes:

- (1) inelastic scattering with cold electrons, which is assumed to "cool" the excited electrons to below the barrier energy and characterized by the scattering length  $L_e$ ;
- (2) elastic scattering with phonons and impurities, characterized by the scattering length  $L_p$ ; and
- (3) diffuse roughness scattering at both front ( $n^+$ - $i$  interface) and back ( $n^+$ -air interface) walls (multiple reflection effect).

For thin  $n^+$  layers, photoemission will be enhanced through the redistribution of momentum by phonon and wall scattering which in fact scatters hot electrons otherwise lost into the set of states within the escape cone. This mechanism has been used to explain the enhanced photoemission observed in thin film Schottky barrier detectors.

In our model, a uniform absorption approximation is used for thin films. In addition, the energy dependence of  $L_e$  and  $L_p$  are ignored. Also we have assumed that the energy losses from electron-phonon collisions are so small that they are negligible.

The fraction of electrons captured prior to any bulk scattering events ( $e$ - $e$  or  $e$ - $p$ ) is given by<sup>19</sup>

$$\eta_0 = \frac{L^*}{W_d} U(W_d/L^*) \eta_{id}, \quad (23)$$

with  $L^* = 1/L_e + 1/L_p$  and  $\eta_{id}$  being the ideal internal quantum efficiency. Here, wall effects are included.  $U(W_d/L^*)$  is

defined by an expression involving well-known exponential integrals which physically represent probabilities of having no bulk collisions in the course of multiple traversals from wall to wall averaged over distance and azimuthal angular parameters (plane-parallel geometry is assumed on the macroscopic level). Approximately we have<sup>18</sup>

$$U(W_d/L^*) \approx [1 - \exp(-W_d/L^*)]^{1/2}, \quad (24)$$

within 10% for  $W_d/L^* \geq 0.20$  and within 5% for  $W_d/L^* \geq 0.35$ . For our case, usually this requirement is satisfied as shown in Sec. V. By taking into account the contributions subsequent to bulk scattering events, the total internal quantum efficiency becomes<sup>19</sup>

$$\eta_i = \frac{\eta_0}{1 - \gamma + \gamma\eta_0/\eta_M}, \quad (25)$$

where  $\gamma = L_e/(L_e + L_p)$  is the probability that an excited electron will collide with a phonon before it collides with a cold electron. Note that as  $L_e \rightarrow \infty$  ( $\gamma \rightarrow 1$ ),  $\eta_i \rightarrow \eta_M$ .

#### D. Barrier collection

A strong bias dependence of spectral response was observed in our previous experiments.<sup>6,7</sup> This phenomenon can be ascribed to the image force effect, which has been used to explain the voltage dependence of photocurrent observed in metal-SiO<sub>2</sub>-Si structures<sup>33</sup> and Schottky barrier detectors.<sup>20</sup> This effect will be described as follows. A photoexcited electron reaching the interface will be injected into the *i* layer, provided that it can reach and surmount the interfacial energy barrier. The ability of an electron to reach the barrier depends on the probability of scattering along the way, and in turn, depends on the distance of the energy barrier from the injecting interface. Both the barrier position and the barrier height are affected by the applied electric field due to the image force effect. As a result, the bias dependence of the photocurrent is determined both by the electron scattering in the image force well and by the image force barrier lowering. The barrier lowering ( $\Delta\phi$ ) and the distance ( $x_m$ ) from the interface to the barrier maximum are given by<sup>34</sup>

$$\Delta\phi = \left( \frac{qF}{4\pi\epsilon_0\epsilon_s} \right)^{1/2}, \quad (26)$$

$$x_m = \left( \frac{q}{16\pi\epsilon_0\epsilon_s F} \right)^{1/2}, \quad (27)$$

where  $F = (V_b - V_0)/W_i$  is the electric field in the *i* region,  $V_b$  the applied bias voltage, and  $V_0$  the flatband voltage.<sup>6</sup>

The escaping electrons are subject to scattering out of the escape cone in passing from the injecting interface to the barrier maximum. The barrier collection efficiency ( $\eta_c$ ) is defined as the probability that an electron travels from the *n*<sup>+</sup>-*i* interface to the barrier maximum without scattering. Since the emitted electrons travel essentially normally to the barrier, in first approximation,  $\eta_c$  is given by<sup>20,33</sup>

$$\eta_c = \exp(-x_m/L_s), \quad (28)$$

in which  $L_s$  is the electron scattering length in the image force well (located in the *i* layer). Here, we have neglected the energy dependence of  $L_s$ . The scattering mechanism is

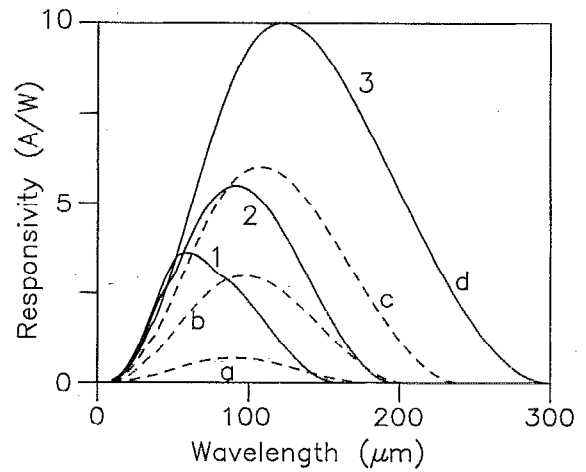


FIG. 4. Spectral response calculated for three detectors with different emitter layer doping concentrations and corresponding optimum thicknesses (solid lines): (1)  $N_d = 1 \times 10^{19} \text{ cm}^{-3}$ ,  $W_d = 540 \text{ \AA}$ ; (2)  $N_d = 2 \times 10^{19} \text{ cm}^{-3}$ ,  $W_d = 180 \text{ \AA}$ ; (3)  $N_d = 3 \times 10^{19} \text{ cm}^{-3}$ ,  $W_d = 100 \text{ \AA}$ . The effect of electric field on spectral response is also shown for detector 3 (dashed lines): (a)  $F = 50 \text{ V/cm}$ , (b)  $F = 200 \text{ V/cm}$ , (c)  $F = 500 \text{ V/cm}$ , (d)  $F = 1000 \text{ V/cm}$ .

assumed to redirect the electron momentum isotropically. If an electron is scattered in the *i* region prior to surmounting the barrier, the electron momentum will be unable to escape without further scattering. It is assumed that no electron is scattered more than once during its passage from the interface to the barrier maximum.

By taking the image force barrier lowering into account, the effective workfunction is  $\Delta = \Delta_0 - \Delta\phi$ , where  $\Delta_0$  is zero field workfunction. This relationship can be used to explain the bias dependence of  $\lambda_c$  observed from experiments.<sup>6,7</sup>

#### V. RESULTS AND DISCUSSIONS

The total quantum efficiency is the product of photon absorption probability, internal quantum efficiency, and barrier collection efficiency,

$$\eta = \eta_a \eta_i \eta_c. \quad (29)$$

The responsivity is given by

$$R = q \eta \lambda / hc. \quad (30)$$

By using the analytic expressions given in the previous sections, the responsivity and quantum efficiency have been calculated for Si *n*<sup>+</sup>-*i* structures, as functions of wavelength, electric field, emitter layer thickness, and doping concentration, etc. Unless indicated otherwise, the following parameters were used in the calculations:  $W_b = 100 \text{ \AA}$ ,  $N_b = 5 \times 10^{18} \text{ cm}^{-3}$ ,  $R_F = 0$ ,  $R_B = 1$ ,  $L_e = 4000 \text{ \AA}$ ,  $L_p = 100 \text{ \AA}$ ,  $L_s = 300 \text{ \AA}$ , and  $F = 1000 \text{ V/cm}$ . For Ge and other III-V compound semiconductors (such as GaAs), in principle, similar analysis can be performed.

The effect of emitter layer doping concentration on spectral response is shown in Fig. 4 (see solid lines). Here three doping concentrations,  $N_d = 1, 2, 3 \times 10^{19} \text{ cm}^{-3}$ , are used with the thicknesses  $W_d = 540, 180, 100 \text{ \AA}$ , respectively, which correspond to the optimum thickness value as discussed in the following paragraph. It can be seen that with

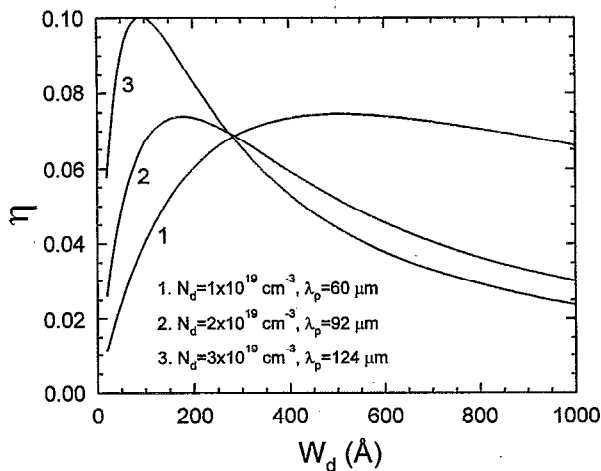


FIG. 5. Quantum efficiency vs emitter layer thickness calculated for different doping concentrations and corresponding peak wavelengths.

the increase of doping concentration, both the spectral bandwidth and the peak responsivity ( $R_p$ ) increase, while the short-wavelength side of the spectral response almost remains the same. The corresponding  $R_p$ ,  $\lambda_c$ ,  $\lambda_p$  (peak wavelength), and  $\Delta\lambda$  (half-peak width) are:  $R_p=3.6, 5.5, 10.0$  A/W,  $\lambda_c=160, 197, 300$   $\mu\text{m}$ ,  $\lambda_p=60, 92, 124$   $\mu\text{m}$ , and  $\Delta\lambda=80, 100, 145$   $\mu\text{m}$ . As analyzed in Sec. IV, the spectral response in the long-wavelength side is governed by the internal photoemission mechanism, while in the short-wavelength side it largely depends on the free-carrier absorption mechanism.

The electric field dependence of spectral response is also shown in Fig. 4 (see dashed lines). As  $F$  increases, both responsivity and  $\lambda_c$  increase considerably due to the image force effect, which is in good agreement with experimental results.<sup>6,7</sup> Also, the peak wavelength shifts gradually to longer wavelengths. In Fig. 4, for a device with  $N_d=3 \times 10^{19}$   $\text{cm}^{-3}$  ( $\Delta_0=7.46$  meV) and  $W_d=100$   $\text{\AA}$ , as  $F$  increases from 50 to 1000 V/cm,  $\Delta$  reduces from 6.7 to 4.0 meV, corresponding to an increase of  $\lambda_c$  from 182 to 300  $\mu\text{m}$ , and  $R_p$  increases from 0.7 to 10.0 A/W with an increase of  $\lambda_p$  from 90 to 123  $\mu\text{m}$ . In order to get a higher responsivity, it seems that the applied bias should be as high as possible. However, in fact, there is an upper limit on applied bias or electric field (represented by  $V_c$  and  $F_c$  respectively), due to the possible impact ionization breakdown of neutral impurity atoms occurring in the  $i$  region. When  $F > F_c$ , the dark current will increase abruptly and the responsivity will decrease rapidly, which has been demonstrated by experimental results.<sup>7</sup> The value of breakdown field in intrinsic (actually  $n^-$  or  $p^-$ ) Si is expected to range from several to a few thousands of V/cm, and is determined by the properties of the residual impurities, such as the impurity ionization energy, the impurity concentration, and the compensation ratio.<sup>35</sup> The curve slope of responsivity vs electric field at a given wavelength is determined by the scattering length ( $L_s$ ) in the image force well. As  $L_s$  increases,  $R$  will increase more rapidly with  $F$ .  $L_s$  is estimated to be around a few

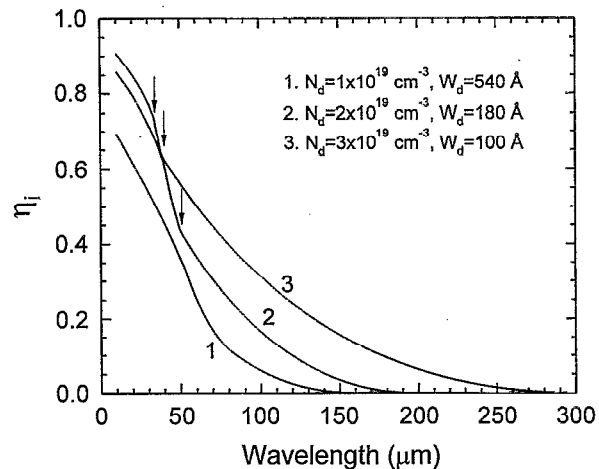


FIG. 6. Internal quantum efficiency vs wavelength calculated for different emitter layer doping concentrations and corresponding optimum thicknesses. The arrows indicate those points at which the curve slopes do not change continuously.

hundreds of  $\text{\AA}$ , which is mainly due to electron-phonon scattering.

Figure 5 shows the emitter layer thickness dependence of quantum efficiency at wavelength around  $\lambda_p$ , for the same three doping concentrations. It is apparent that for different doping concentrations (i.e., different  $\lambda_c$ ), there exist different optimum emitter layer thickness ranges within which the quantum efficiency reaches a maximum. With the increase of  $N_d$ , the optimum  $W_d$  reduces and the effective thickness range becomes narrow, but the peak quantum efficiency increases. As shown in Fig. 5, for  $N_d=1, 2, 3 \times 10^{19}$   $\text{cm}^{-3}$ , the optimum  $W_d$  is around 540, 180, 100  $\text{\AA}$ , and the peak  $\eta$  reaches 7.5%, 7.4%, 10.0%. When  $W_d$  is larger than the optimum thickness,  $\eta$  becomes small due to the hot-electron scattering. When  $W_d$  is smaller than the optimum thickness,  $\eta$  also decreases due to the reduction of photon absorption in the emitter layer. As a result, the optimum thickness is a tradeoff of these two processes (absorption and scattering). The optimum thickness can be found from a 3D plot of responsivity as a function of wavelength and emitter layer thickness.

It is also noted from Fig. 5 that for those thicknesses at which the internal photoemission mechanism is dominant,  $\eta$  decreases with the increase of doping concentration. This is due to the fact that the ratio of workfunction to Fermi energy ( $\Delta/E_F$ ) decreases with increasing doping concentration, as can be seen in Fig. 2, such that more photoexcited electrons will not gain sufficient energy to overcome the barrier. Due to the same reason, the turn-on part of spectral response becomes less sharp for longer-wavelength detectors, as shown in Fig. 4. The wavelength dependence of  $\eta_i$  for different doping concentrations is more clearly shown in Fig. 6. It is noted that within some wavelength ranges the slope of  $\eta_i$  vs  $\lambda$  curve does not change continuously as pointed out by arrows. This is because in different photon energy ranges, such as  $\Delta < h\nu < E_F$ ,  $E_F < h\nu < E_F + \Delta$ , and



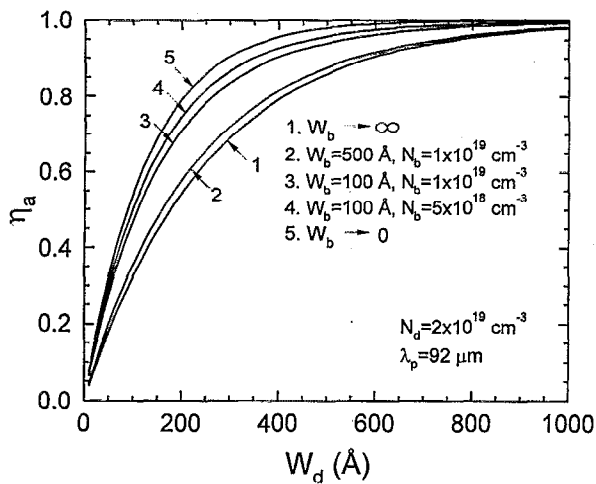


FIG. 7. Photon absorption probability vs emitter layer thickness calculated for different bottom contact layer thicknesses and doping concentrations.

$h\nu > E_F + \Delta$ ,  $\eta_i$  has a different function relationship with photon energy as given in Sec. IV B.

The bottom contact layer has a serious effect on quantum efficiency as shown in Fig. 7. It is seen that with the increase of  $W_b$  or  $N_b$ , the absorption efficiency reduces considerably, especially for thin emitter layer thicknesses which are required by the optimization of quantum efficiency. Thus the fabrication of transparent or semitransparent contact layers is a challenge for designing this kind of FIR detectors. A better method is to use multilayer structure to get most of the incident photons absorbed in the emitter layers. In this way, the photon absorption efficiency will increase greatly. Another advantage for using multilayer structures is the exploitation of possible photocurrent gain mechanisms,<sup>8</sup> which will further increase the responsivity.

The effects of hot-electron elastic and inelastic scattering lengths on the internal quantum efficiency are also studied. At present time, no data are available for these scattering lengths in heavily doped Si at low temperatures. However, due to the low hot-electron energy (ranging from several to several tens of meV) encountered in our FIR detectors and the very low-temperature operation (near 4.2 K), the values of  $L_e$  and  $L_p$  for our case should be larger than those for Schottky barrier detectors.<sup>19</sup> Thus, a reasonable range can be assumed. For  $L_p$ , it may be from several tens to a few hundreds of Å, while for  $L_e$ , it may be from several thousands of Å to a few μm. Calculated results show that as  $L_e$  increases or  $L_p$  decreases,  $\eta_i$  increases. The decrease of  $L_p$  increases the chance for hot electrons to be redirected into the escape cone.

## VI. SUMMARY

We have shown that homojunction internal photoemission (HIP) detectors can be classified into three types in terms of the doping concentration in the emitter layer: type-I ( $N_d < N_c$ ), type-II ( $N_c < N_d < N_0$ ), and type-III ( $N_d > N_0$ ). Their photoresponse mechanisms have been distinguished and compared. Using the type-II structure, we may realize

high performance Si FIR detectors ( $\lambda_c > 40 \mu\text{m}$ ). In principle,  $\lambda_c$  can be tailored to any value by changing the doping concentration. An analytic expression from the high-density theory has been used to obtain the  $\lambda_c$  vs  $N_d$  relationship. An analytic model has been introduced to describe electron photoemission processes, which include photoexcitation due to free-carrier absorption, ideal internal photoemission, hot-electron transport, and interfacial barrier collection due to the image force effect. For Si  $n^+i$  structures, the effects of doping concentration, emitter layer thickness, applied bias voltage (electric field), electron scattering lengths, and bottom contact layer, on photoresponse performance (spectral response and quantum efficiency), have been calculated. Our modeling results are qualitatively in agreement with experimental results obtained from commercial samples. These results should be useful for the design and optimization of type-II HIP detectors.

Our results show that even for the single-layer structure a quantum efficiency of about 10% may be reached. To obtain the maximum quantum efficiency, an optimum emitter layer thickness exists, which ranges from several tens to several hundreds of Å depending on the doping concentration (hence  $\lambda_c$ ). By using multilayer structures ( $n^+i-n^+i\dots$  or  $p^+i-p^+i\dots$ ), which can be realized by MBE or MOCVD growth technologies, it is expected that the quantum efficiency may be further increased due to the increased photon absorption efficiency and possible photocurrent gain enhancement.

In this paper, we do not consider the dark current (and noise), which is another important figure of merit to represent the detector performance. Preliminary results obtained<sup>6</sup> show that the forward dark current, mainly due to the thermionic emission process, can be very small at low temperatures.

Although we have presented an analytic model to predict the photoresponse performance of our type-II detectors, several problems still exist, which are either neglected or overcome by using assumptions, as discussed in above sections. These problems are summarized as follows:

- (1) the doping concentration dependence of workfunction in the moderate doping range;
- (2) the relationship of FIR absorption coefficient ( $\lambda > 40 \mu\text{m}$ ) with wavelength and doping concentration in heavily doped semiconductors;
- (3) the values of electron elastic and inelastic scattering lengths and their energy dependence, both in the emitter layer and in the image force well ( $i$  layer);
- (4) the effect of different dopants on the detector performance. To solve these problems, more experimental and theoretical work is needed.

## ACKNOWLEDGMENTS

This work was supported in part by the NSF under Grant No. ECS-94-12248. The authors would like to acknowledge Dr. H. C. Liu for many fruitful discussions and Steven Matsik for his technical help.

- <sup>1</sup>M. W. Werner and M. Bothwell, presented at Infrared/Submillimeter Astronomy Symposium, COSPAR/World Space Congress, September 1992.
- <sup>2</sup>E. E. Haller, M. R. Hueschen, and P. L. Richards, *Appl. Phys. Lett.* **34**, 495 (1979).
- <sup>3</sup>D. M. Watson and J. E. Huffman, *Appl. Phys. Lett.* **52**, 1602 (1988).
- <sup>4</sup>I. C. Wu, J. W. Beeman, P. N. Luke, W. L. Hansen, and E. E. Haller, *Appl. Phys. Lett.* **58**, 1431 (1991).
- <sup>5</sup>N. Sclar, *Prog. Quantum Electron.* **9**, 149 (1984).
- <sup>6</sup>D. D. Coon, R. P. Devaty, A. G. U. Perera, and R. E. Sherriff, *Appl. Phys. Lett.* **55**, 1738 (1989).
- <sup>7</sup>A. G. U. Perera, R. E. Sherriff, M. H. Francombe, and R. P. Devaty, *Appl. Phys. Lett.* **60**, 3168 (1992).
- <sup>8</sup>A. G. U. Perera, J.-W. Choe, M. H. Francombe, R. E. Sherriff, and R. P. Devaty, *Superlattices and Microstructures* **14**, 123 (1993).
- <sup>9</sup>H. C. Liu, J.-P. Noel, Lujian Li, M. Buchanan, and J. G. Simmons, *Appl. Phys. Lett.* **60**, 3298 (1992).
- <sup>10</sup>N. M. Haegel, *J. Appl. Phys.* **64**, 2153 (1988).
- <sup>11</sup>A. G. U. Perera, H. X. Yuan, M. H. Francombe, and J.-W. Choe, Proceedings of the Electrochemical Society Symposium on LWIR Detectors and Arrays, New Orleans LA, Oct 11-15, 1993.
- <sup>12</sup>F. D. Shepherd, *Proc. SPIE* **1735**, 250 (1992).
- <sup>13</sup>W. F. Kosonocky, *Proc. SPIE* **1685**, 2 (1992).
- <sup>14</sup>T. L. Lin and J. Maserjian, *Appl. Phys. Lett.* **57**, 1422 (1990).
- <sup>15</sup>B.-Y. Tsaur, C. K. Chen, and S. A. Marino, *Proc. SPIE* **1540**, 580 (1991).
- <sup>16</sup>S. Tohyama, N. Teranishi, K. Konuma, M. Nishimura, K. Asai, and E. Oda, *IEDM Tech. Dig.*, 1988, p. 82.
- <sup>17</sup>V. L. Dalal, *J. Appl. Phys.* **42**, 2274 (1971).
- <sup>18</sup>V. E. Vickers, *Appl. Opt.* **10**, 2190 (1971).
- <sup>19</sup>J. M. Mooney and J. Silverman, *IEEE Trans. Electron Devices* **ED-32**, 33 (1985).
- <sup>20</sup>J. M. Mooney, *J. Appl. Phys.* **65**, 2869 (1989).
- <sup>21</sup>D. E. Mercer and C. R. Helms, *J. Appl. Phys.* **65**, 5035 (1989).
- <sup>22</sup>S. C. Jain, R. P. Mertens, and R. J. Van Overstraeten, in *Advances in Electronics and Electron Physics*, edited by P. W. Hawkes (Academic, New York, 1991), Vol. 82, p. 197.
- <sup>23</sup>S. C. Jain and D. J. Roulston, *Solid-State Electron.* **34**, 453 (1991).
- <sup>24</sup>J. S. Escher, in *Semiconductors and Semimetals*, edited by R. K. Willardson and A. C. Beer (Academic, New York, 1981), Vol. 15, p. 195.
- <sup>25</sup>M. D. Petroff and M. G. Stapelbroek, U. S. Patent No. 4 568 960 (4 Feb. 1986).
- <sup>26</sup>F. Szmulowicz and F. L. Madarsz, *J. Appl. Phys.* **62**, 2533 (1987).
- <sup>27</sup>G. D. Mahan, *J. Appl. Phys.* **51**, 2634 (1980).
- <sup>28</sup>N. F. Mott, *Metal-Insulator Transitions* (Barnes and Noble, New York, 1974).
- <sup>29</sup>J. R. Klauder, *Ann. Phys.* **14**, 43 (1961).
- <sup>30</sup>D. K. Schroder, R. N. Thomas, and J. C. Swartz, *IEEE Trans. Electron Devices* **ED-25**, 254 (1978).
- <sup>31</sup>R. A. Smith, *Semiconductors* (Cambridge, London, 1978), p. 294.
- <sup>32</sup>R. Williams, in *Semiconductors and Semimetals*, edited by R. K. Willardson and A. C. Beer (Academic, New York, 1970), Vol. 6, p. 97.
- <sup>33</sup>C. N. Berglund and R. J. Powell, *J. Appl. Phys.* **42**, 573 (1971).
- <sup>34</sup>S. M. Sze, *Physics of Semiconductor Devices*, 2nd ed. (Wiley, New York, 1981), p. 250.
- <sup>35</sup>P. R. Bratt, in *Semiconductors and Semimetals*, edited by R. K. Willardson and A. C. Beer (Academic, New York, 1977), Vol. 12, p. 39.